CrystEngComm

PAPER

Cite this: *CrystEngComm*, 2014, **16**, 9482

GISAXS and GIWAXS study on self-assembling processes of nanoparticle based superlattices†

M. Corricelli,‡[ab] D. Altamura,‡[c] M. L. Curri,[b] T. Sibillano,[c] D. Siliqi,[c] A. Mazzone,[c] N. Depalo,[b] E. Fanizza,[ab] D. Zanchet,[d] C. Giannini*[c] and M. Striccoli*[b]

Received 25th June 2014,
Accepted 13th August 2014

DOI: 10.1039/c4ce01291g

www.rsc.org/crystengcomm

Organic capped Au nanoparticles (NPs) and PbS quantum dots (QDs), synthesized with high control on size and size distribution, were used as building blocks for fabricating solid crystals by solvent evaporation. The superlattice formation process for the two types of nano-objects was investigated as a function of concentration by means of electron microscopy and X-ray techniques. The effect of building block composition, size, geometry, and concentration and the role of the organic coordinating molecules was related to the degree of order in the superlattices. A convenient combination of different complementary X-ray techniques, namely *in situ* and *ex situ* GISAXS and GIWAXS, allowed elucidating the most reliable signatures of the superlattices at various stages of the self-assembly process, since their early stage of formation and up to few months of aging. Significantly different assembly behaviour was assessed for the two types of NPs, clearly explained on the basis of their chemical composition, ultimately reflecting on the assembling process and on the final structure characteristics.

Introduction

Nanoparticle (NP) assemblies have been attracting growing interest as a versatile bottom-up approach for design of functional materials with tailored properties. In the past decades, significant advances have been made in NP synthesis. In particular, colloidal synthetic routes have resulted in an accurate control on sizes, shapes, and surface chemistry of a wide variety of high-quality organic capped metal, semiconductor and oxide NPs and quantum dots (QDs), thus making available a wide range of nano-sized building-blocks with carefully tunable physical and chemical properties. The ability to assemble NPs and QDs as artificial atoms, into desired and highly ordered architectures, allows a rational control of the electronic, plasmonic, and/or magnetic coupling between such artificial atoms.

NPs have been organized in films exploiting a plethora of approaches, which ranges from simple drop casting,[1] to Langmuir–Blodgett deposition technique,[2] or doctor blade casting.[3] Among these, self-assembly of nano-objects by solvent evaporation of a drop cast dispersion of NPs provides a simple and low-cost method for producing NP ensembles with a large extension, with interparticle distances comparable with the NP size. In this case, ordering, achieved by solvent evaporation, causes a gradual increase of the NP volume fraction until the NP superlattice nucleates, thus forming an ordered equilibrium superstructure. This hierarchical organization of NPs can be successfully controlled by carefully tailoring parameters such as NP size, size distribution and concentration, as well as dispersing solvent, evaporation temperature and chemistry of the supporting substrate. When a suitable combination of experimental parameters is selected, the solvent evaporation process will evolve under thermodynamic control and, as soon as the attraction energy (ascribed to covalent or hydrogen bonding, electrostatic attraction between oppositely charged ligands, depletion forces or dipole–dipole interactions) is comparable to that of repulsive forces (such as steric forces and electrostatic repulsion between ligands with the same charge),[4] a regular NP organization will be obtained.[5]

[a] *Dipartimento di Chimica, Università degli Studi di Bari, Via Orabona 4, I-70126, Bari, Italy*

[b] *Istituto per i Processi Chimico Fisici (IPCF-CNR) Bari, c/o Dipartimento di Chimica, Università degli Studi di Bari, Via Orabona 4, I-70126, Bari, Italy. E-mail: m.striccoli@ba.ipcf.cnr.it*

[c] *Istituto di Cristallografia (IC-CNR), Via Amendola 122/O, I-70126, Bari, Italy. E-mail: cinzia.giannini@ic.cnr.it*

[d] *Instituto de Química-UNICAMO, C.P. 6154, 13083-970, Campinas, SP, Brazil*

† Electronic supplementary information (ESI) available: Additional TEM micrographs of PbS QDs, full range GISAXS 2D maps collected on PbS QD aged *assemblies*, GISAXS experimental pattern of a 3×10^{-9} M $PbS_{2.7}$ sample (aged *solution*), both indexed as fcc superlattice and with the different SL orientations. Movies of the as-collected *in situ* data for Au NPs drop-cast from solutions with concentrations equal to 2.5×10^{-8} M (Movie 1), 7.5×10^{-8} M (Movie 2) and 1.5×10^{-7} M (Movie 3), for $PbS_{2.7}$ QDs drop-cast from solutions with concentrations equal to 3×10^{-7} M (Movie 4), 5×10^{-7} M (Movie 5) and 7×10^{-7} M (Movie 6) and for $PbS_{3.3}$ QDs drop-cast from solutions with concentrations equal to 3×10^{-7} M (Movie 7), 5×10^{-7} M (Movie 8) and 7×10^{-7} M (Movie 9). See DOI: 10.1039/c4ce01291g

‡ These authors contributed equally to this work.

Interestingly, the resulting NP superstructures are characterized by unique chemical and physical properties, also different from the ones of single NPs and the corresponding bulk materials. The capacity to self-assemble can greatly facilitate the integration of nano-objects in different technological processes, including microscale fabrication, for a wide range of applications, such as electronics,[6] sensors[7] and optical devices.[8] For example, thiolate-passivated gold and silver nanocolloids have been organized by means of layer-by-layer assembly, showing strong transverse (intralayer) and longitudinal (interlayer) near-field coupling.[9] Also, a simple solvent evaporation strategy has been used for organizing Au NPs in a 2D superlattice with a highly controlled geometry and extending over μm^2, showing plasmonic properties strongly depending on the chemistry of the supporting substrate, which was found to influence NP ordering and near-field interactions between NPs.[10] In the case of close-packed semiconductor PbS QDs, the energy coupling between neighboring nano-objects has been found to be dependent on both the interparticle distance and the QD size.[11] Moreover, cascade energy transfer has been observed in structures made of layer-by-layer assembled CdTe QDs, organized accordingly to a funnel-like band gap profile, thus obtaining a system potentially useful for tunable lasers.[12]

Furthermore, the geometric characteristics of the NP organization determine the collective properties arising from the NP superstructure, therefore a comprehensive knowledge of NP organization mechanism is fundamental for engineering such superstructures. In organic capped NPs and QDs, an important role is played by the coordinating organic molecules, that not only protect NPs from coalescence, but may act also as active bonds for forming superlattice structures. In addition, an adjustable interparticle distance can possibly result in tunable electric, optical and transport properties. Indeed, attention is now focused on a deeper understanding of factors that control the self-assembly and a comprehensive characterization of NP arrays, at various stages of the self-assembly process, represents a fundamental study.

Scanning (SEM) and transmission electron microscopy (TEM) are very powerful techniques for NP and NP superstructure investigation, as they provide information on NP shape, average size and size distribution. However, the information is usually obtained after numerical evaluation of real space micrographs from limited data sets. In addition, in most of cases limitations come from the fact that only a two-dimensional (2D) description can be obtained, thus missing the information contained in the direction perpendicular to the sampling substrate.

The combination of electron microscopy techniques with grazing incidence small-angle X-ray scattering (GISAXS) revealed a powerful tool for the study of NP self-assembly. GISAXS allows to monitor the NP arrangement, and to investigate the self-assembled arrays on solid surfaces. In GISAXS measurements, an X-ray beam is incident upon the NP organization on the supporting substrate, at an angle which allows to maximize the interaction of the beam with the nanostructured film. A precise fitting of the measured GISAXS data may encode information, such as the NP size and size dispersion as well as the interparticle distance which is affected by the surfactant shell.

Furthermore, *in situ* GISAXS enables the investigation of rapid self-assembly processes in films, under ambient conditions, for the direct *in situ* tracking of the process underlying the NP organization upon solvent evaporation. The knowledge of the mechanism underlying the NP organization plays an important role in both fundamental studies and applied research. Many examples have been reported of *in situ* GISAXS investigations coupled to TEM/SEM studies of the NP self-assembly process. For example, a time-resolved GISAXS study has been carried out to study the self-assembly process of iron oxide NPs, finding a NP hexagonal arrangement and that the organization occurs in the vicinity of the three-phase drop contact line.[13] Also, combining GISAXS and TEM, a study on the self-assembly of CdSe/CdS nanorods at the liquid/air interface has been reported, showing that the nanostructure was formed at this interface.[14]

In this work, a combined approach of *ex situ* electron microscopy with *in situ* GISAXS investigation was employed for the study of the mechanism underlying the formation of NP assembly upon a slow solvent evaporation, as a function of NP concentration. In particular, organic capped Au NPs and PbS QDs self-assembly was considered to investigate possible effects of NP chemical composition on the overall self-assembly formation process. The assembly process was carried out at room temperature, in open air conditions, and investigated by combining *in situ* and *ex situ* GISAXS and *ex situ* wide angle X-ray scattering (GIWAXS). The overall ensemble of experiments aimed at elucidating the assembly evolution along various stages of the process, since their early stage of superstructure formation. The structural investigation allowed studying aging effect on symmetry and stability of the superlattices, as well as the *orientational* ordering of the building blocks.

Experimental

Materials

Lead(II) oxide (PbO, powder 99.99%), hexamethyldisilathiane (HMDS, synthesis grade), 1-octadecene (ODE, 90% technical grade), oleic acid (OAc, technical grade 90%), trioctylphosphine (TOP, 90% technical grade), hydrogen tetrachloroaurate(III) trihydrate ($HAuCl_4 \cdot 3H_2O$, 99.999%), oleylamine (OAm, technical grade 70%) and solvents, namely toluene and nonane (of the highest purity available) were purchased by Sigma Aldrich and were used without further purification.

Au nanoparticle and PbS quantum dot synthesis and characterization

Spherical OAm-coated Au nanoparticles (NPs) were prepared by following a versatile reported method with minor modifications.[15,16] In a typical experiment, OAm was heated at

130 °C under vacuum and purified prior to use. A mixture of Au precursor ($HAuCl_4 \cdot 3H_2O$, 60 mg), and OAm (1.3 g) was dissolved in toluene (1 mL) and injected into a three neck flask containing a refluxing solution of OAm (2.5 g) in 49 mL of toluene. The OAm acts both as reducing agent during the NP growth and coordinating molecule at the end of the synthesis. Upon injection and heating at high temperature (100 °C), the reaction mixture colour changes from orange to bright yellow, becoming then colourless, due to reduction of Au(III) to Au(I) and gradually turns into deep red, indicating the formation of Au NPs. The particle growth was monitored by absorption spectroscopy and the reaction was stopped after two hours. The as-prepared colloidal dispersion in toluene was firstly centrifuged to remove larger metal particle aggregates and then used for a subsequent Au NP size sorting treatment, which was carried out in order to improve the Au NP size distribution. Such a size sorting treatment consisted in an antisolvent centrifugal precipitation based on the addition of a suitable volume of an antisolvent (methanol) to a defined volume of as synthesized Au NP dispersion and by repeated cycle of antisolvent addition/centrifugation. Briefly, an appropriately defined volume of methanol (1.5 mL) was added to the NP solution (6 mL). Upon centrifugation at 950 g for 10 min a partial amount of NPs was precipitated and collected and redispersed in organic solvent (nonane). The NP concentration was obtained by calculating the extinction coefficient of OAm-capped Au NPs in nonane, according to the approach described by Liu *et al.*[17] Au NP solution with three different concentrations were prepared, namely equal to 2.5×10^{-8} M, 7.5×10^{-8} M and 1.5×10^{-7} M, respectively.

The preparation of PbS QDs was carried out as previously reported.[18] In a typical synthesis, 4 mmol of PbO, 3.0 mL of TOP, and 2.5 mL of OAc were added to 36 mL of ODE, a non-coordinating solvent, and stirred under vacuum at 120 °C: at this stage the formation of lead-oleate precursors occurred. Subsequently, a 20 mM solution of the sulphur precursor, HMDS in ODE, was swiftly injected, corresponding to a Pb/S molar ratio equal to 2 : 1, followed by the cooling down to 80 °C, in order to interrupt the nucleation phase and let the just formed nuclei to grow. The reaction was stopped after 5 min and 7 min, for obtaining PbS QDs with a diameter equal to about 2.7 nm and 3.3 nm, respectively. The obtained QDs were purified by using a non-solvent precipitation procedure, carried out by adding to the reaction product a large amount of ethanol. To completely remove the excess of OAc and other impurities formed during the reaction, up to 3 centrifugation steps were required, finally yielding a powder. The obtained precipitate was then dispersed in toluene. For both PbS QD sizes, solutions with different concentration were prepared, namely equal to 3×10^{-7} M, 5×10^{-7} M, 7×10^{-7} M, 3×10^{-8} M, 3×10^{-9} M and 3×10^{-10} M, respectively. In addition, for both PbS QD sizes, aged samples were also investigated, particularly focusing on the assemblies after 7 months of aging in air (aged *assemblies*) and assemblies prepared by drop casting the same original solution used for the earlier samples (with concentrations equal to 3×10^{-8} M, 3×10^{-9} M and 3×10^{-10} M), kept for 7 months in a closed vial (aged *solutions*).

The absorption spectra of Au NPs and of PbS QDs were recorded on samples purified and redispersed in nonane and toluene, respectively, by means of a Cary Varian 5000 UV-visible-NIR spectrophotometer. Transmission Electron Microscopy (TEM) analyses were performed by using a Jeol-Jem 1011 microscope, working at an accelerating voltage of 100 kV. TEM images were acquired by a Quemesa Olympus CCD 11 Mp Camera. The samples for TEM investigation were prepared by dipping the 300 mesh carbon-coated Cu grid in the nonane solution of Au NPs. Alternatively, 10 μL of toluene PbS QD solutions with concentration values equal to 3×10^{-7} M, 5×10^{-7} M, 7×10^{-7} M and for both QD sizes, were drop-cast on the TEM grids. The solvent was allowed to evaporate before the analyses. Infrared spectra were recorded with a Perkin-Elmer Spectrum One Fourier transform infrared (FTIR) spectrometer equipped with a DTGS (deuterated triglycine sulphate) detector. The spectral resolution used for all experiments was 4 cm^{-1}. For attenuated total reflection (ATR) measurements, the internal reflection element (IRE) was a three-bounce, 4 mm diameter diamond microprism. The film samples were directly cast onto the internal reflection element by depositing the solution of interest (10 μL) on the upper face of the diamond crystal and allowing the solvent to evaporate completely.

Au NP and PbS QD superlattice: formation and characterization

120 μL of OAm-capped Au NP and OAc/TOP-capped PbS QD solutions were drop-cast on 1 × 1 cm silicon substrates. Particularly, Au NP solutions in nonane with different concentrations were drop-cast and the solvent evaporation was carried out at 40 °C. For both ~2.7 nm and ~3.3 nm PbS QDs, the QD dispersions in toluene with different concentrations were drop-cast and the solvent was let to evaporate at room temperature.

Field emission SEM (FE-SEM) measurements were performed by means of a Zeiss Sigma microscope operating in the range 0.5–20 kV. Samples were set onto stainless-steel stub sample holders, by double-sided carbon tape.

In situ GISAXS measurements were performed at the XRD2 beamline at LNLS (Brazilian Synchrotron Light Laboratory) in Campinas (Brazil). A Pilatus 100 K detector was used, having 487 × 195 pixels, and 172 μm × 172 μm pixel size. The sample-to-detector distance was equal to 484 mm; the radiation wavelength was λ = 0.155 nm and the incidence angle α_i = 0.17°.

The colloidal solutions were manually dropped on silicon substrates and let evaporate in open air, while collecting the GISAXS signal. Substrates were first aligned in the X-ray beam prior to dropping the solution; data collection was started approximately 30 s later. Each data frame was saved after 10 s collection time, for a total acquisition time of 120 min for Au NPs and 30 min for PbS QDs, respectively. *Ex situ* GISAXS

and GIWAXS measurements on the aged samples were performed on a laboratory (GI)SAXS/(GI)WAXS set-up (XMI-Lab[19]). Particularly, for both PbS QD sizes, 7 months aged *assemblies* and aged *solutions* (with concentrations equal to 3×10^{-8} M, 3×10^{-9} M and 3×10^{-10} M) were investigated. The experimental settings were: 0.18° incidence angle and 0.154 nm radiation wavelength. GISAXS data were collected on a multiwire or on an image plate detector at 2070 mm or 180 mm sample-to-detector distance, respectively. GIWAXS data were collected on the image plate detector at ~90 mm far from the sample.

Results

OAm-capped Au NPs and OAc/TOP-capped PbS QDs were synthesized with a high control on size and surface chemistry. The two types of nano-objects were purposely selected to investigate systems with significantly different electronic properties, metal and semiconductor respectively, but characterized by surface coordinating agents having the same alkyl chain, thus providing convenient systems to be compared in the formation of self-assemblies by solvent evaporation.

Au NP synthesis and characterization

Au NPs, characterized by a very narrow size-distribution, were successfully prepared by combining a colloidal synthetic strategy with an effective post-preparative size sorting procedure, based on an antisolvent (methanol) centrifugal fractional precipitation. The corresponding TEM micrograph, reported in Fig. 1a, shows spherical NPs, with a size equal to D_{Au} = 11.7 ± 0.7 nm, thus confirming the NP very narrow size distribution. In Fig. 1b is reported the UV-vis absorption spectrum of the resulting Au NPs dispersed in nonane. The characteristic localized surface plasmon resonance (LSPR) band is clearly visible at 525 nm, in agreement with the size measured by TEM investigation.

PbS QD synthesis and characterization

OAc/TOP-capped PbS QDs were prepared by following a colloidal synthetic procedure in hot coordinating solvent, which allows to control the QD final size by carefully modulating the growth time. Two sets of size-monodispersed PbS QDs with average QD size of 2.7 ± 0.4 nm and 3.3 ± 0.4 nm, indicated in the following as $PbS_{2.7}$ and $PbS_{3.3}$ respectively, were synthesized (Fig. 1c and d, respectively). The size of the QDs was measured by TEM, resulting in a good agreement with the value, calculated from the optical absorption spectrum[20] in toluene solution, using the spectral position of the first 1S excitonic features at 831 nm and 994 nm, respectively (see Fig. 1e).

Au NP and PbS QD surface chemistry characterization

FTIR-spectroscopy in ATR mode was carried out on both Au NPs and $PbS_{2.7}$ QDs, to investigate their surface chemistry.

In Fig. 2 the ATR-FTIR spectra of OAm, OAm-capped Au NPs, OAc and OAc/TOP-capped PbS QDs are reported. All the spectra clearly present two strong bands and one weaker band in the range between 2850 and 3000 cm^{-1} (Fig. 2a, blue box), which can be undoubtedly ascribed to the stretching vibrations of C–H bonds of CH_3, CH_2 and CH moieties belonging to the long alkyl chains of OAm, OAc and TOP molecules. In addition, both the weak band in the range 1463–1467 cm^{-1} (Fig. 2a, orange box) and at 725 cm^{-1} (Fig. 2a, green box) can be ascribed to bending vibrations of

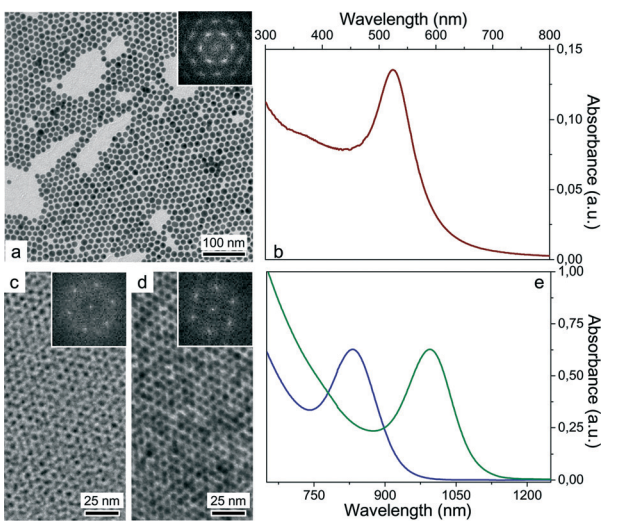

Fig. 1 TEM micrograph (a), corresponding FFT (a, inset) and UV-vis absorption spectrum of Au NPs in nonane (b). TEM micrograph (c, d), corresponding FFT (c and d, inset) and vis-NIR absorption spectra of $PbS_{2.7}$ (blue line) and $PbS_{3.3}$ (green line) in nonane, respectively (e).

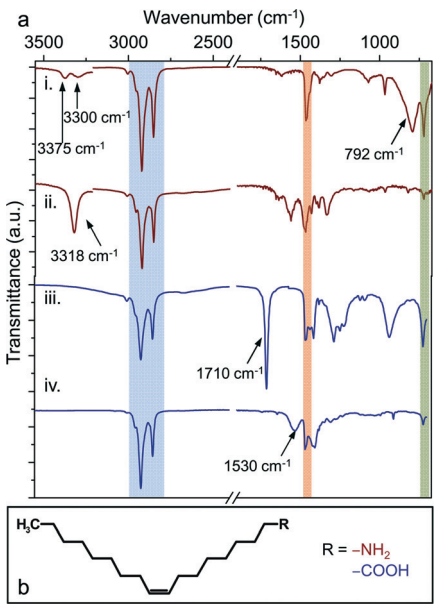

Fig. 2 (a) ATR-FTIR spectra of i. OAm, ii. OAm-capped Au NPs, iii. OAc, iv. OAc/TOP-capped PbS QDs. For the sake of clarity, the transmittance has been multiplied by 2 in the regions 4000–3210 cm^{-1} and 1900–700 cm^{-1}. (b) Structure formula of OAm and OAc molecules.

C–H bonds in CH_2 groups, and particularly to deformation and rocking vibrations, respectively.

In addition, focusing on OAm-capped Au NP spectrum (Fig. 2a(ii)), the characteristic vibrational modes of $-NH_2$ group as a single band at 3318 cm^{-1} can be detected, instead of the typical double band recorded in the pure OAm spectrum (3375 and 3300 cm^{-1}, Fig. 2a(i)). Moreover, the wagging vibration of N–H (792 cm^{-1}), which can be detected in the OAm spectrum (Fig. 2a(i)), disappears in the Au NP spectrum (Fig. 2a(ii)), thus suggesting the coordination of the $-NH_2$ groups to the NP surface. Also the stretching modes characteristic of oxidized $-NH_2$ groups (–CN and imine) can be identified in the spectrum (1650 and 1562 cm^{-1}), confirming the OAm role as reducing agent, but indicating also that nitrile and imine groups can act as ligands for the NPs.[16]

The pure OAc spectrum (Fig. 2a(iii)) presents a broad band between 3500 cm^{-1} and 2500 cm^{-1}, ascribable to the O–H stretching of the carboxylic group. The intense peak at 1710 cm^{-1} and the band at 1284 cm^{-1} are ascribable to C═O and C–O stretching, respectively. The bands at 1412 cm^{-1} and at 935 cm^{-1} can be assigned to the O–H in-plane and out-of-plane stretching, respectively. The PbS QD spectrum (Fig. 2a(iv)) clearly lacks the C–OH vibrations, thus suggesting an interaction between the carboxylic moiety of OAc molecules and the PbS QD surface through a bidentate bond, as confirmed by the appearance of the stretching of the COO^- group at 1530 cm^{-1}.[21] No distinctive vibrations can be univocally ascribed to the coordination of the TOP molecule to the QD surface, as the only characterizing vibration of a trialkylphosphine is the P–CH_2 vibration, which typically lies above 1400 cm^{-1}, that is a region very crowded due to aliphatic chain signals. However, previous works demonstrated the coordination of TOP to the surface of PbS QDs obtained in similar conditions, binding to the QD surface at sulphur sites.[22,23]

FTIR analysis thus confirms that the organic capped Au NPs and PbS QDs, present a similar surface chemistry, having OAm and OAc the same long alkyl chain and differing only for the functional group coordinating the NP surface (Fig. 2b).

In situ GISAXS investigation of Au NP superlattices

Nonane solutions of OAm-capped Au NPs, with 11.7 nm average diameter (D_{Au}), at three increasing concentrations equal to 2.5×10^{-8} M, 7.5×10^{-8} M and 1.5×10^{-7} M, respectively, were deposited on silicon substrates and let evaporate in open air. In the meantime the GISAXS signals were collected every 10 s for a total acquisition time of 120 min. The earliest frame featuring any scattering signal for increasing concentration was observed after *ca.* 40 min, 50 min and 60 min, respectively (ESI,† Movies 1, 2 and 3). The obtained assemblies were investigated also by SEM. The SEM micrographs, along with the last collected frames of the GISAXS measurements, are shown in Fig. 3 (left and right column, respectively).

SEM pictures show a larger coverage of the substrate at increasing NP concentration in solution. Such a finding is in

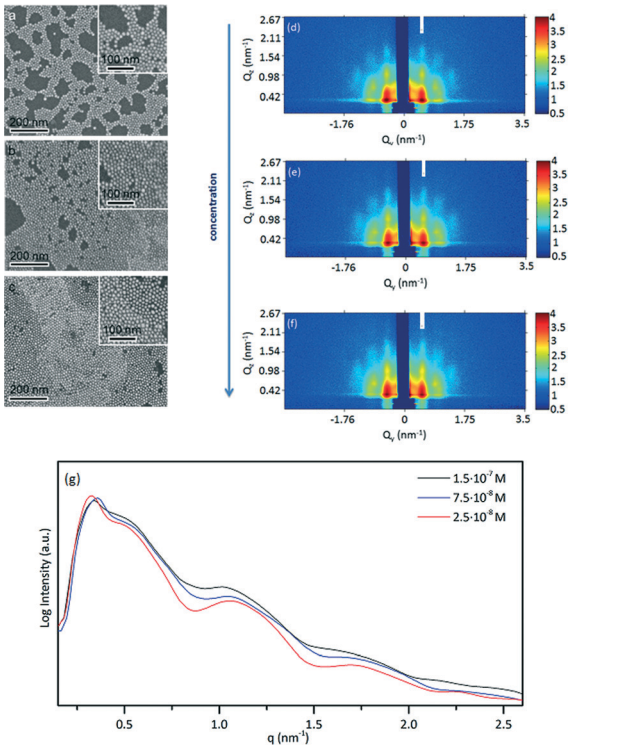

Fig. 3 (a–c) FE-SEM micrographs of Au NP assemblies at concentration of 2.5×10^{-8} M, 7.5×10^{-8} M and 1.5×10^{-7} M, respectively; (d–f) corresponding GISAXS experimental patterns (last frame of the *in situ* acquisition), (g) 1D profiles taken along the vertical direction marked by the white ticks in the 2D maps.

agreement with GISAXS measurements (Fig. 3d–f) that evidence in the colour maps, along with the superlattice formation, an increase of intensity of GISAXS signals with concentration. Such an increase can be also observed in the 1D profiles, reported in Fig. 3g, taken along the directions marked by the white ticks in the GISAXS maps (which are on the same scale). Indeed the collected GISAXS maps show characteristic features of 2D in plane assemblies, as demonstrated in a previous work:[10] in such a case, the scattering intensity modulation in a direction parallel to Q_z is dominated by the form factor, *i.e.* by the scattering contribution due to particle morphology. In particular, the mutual distance between intensity maxima (or minima) is directly related to particle size (D_{Au}). As a consequence, while the trend of the three 1D cuts in Fig. 3g is basically independent from the particle concentration, as expected, a slight increase of the overall intensity with concentration is observed, instead, ascribable to the increasing number of scattering particles. The superlattice symmetry, approximately hexagonal with average lattice parameter a = 15 nm, as previously reported,[10] was found not to change as a function of concentration (*i.e.* the distribution of the scattering intensity parallel to Q_y is also independent of particle concentration). At increasing concentration of the drop cast NP solution, the assembly is seen to proceed in 2D layers parallel to the substrate plane, without the formation of packed 3D

nanostructures. The formation of few islands of multilayered NPs is also observed at higher concentration.[10] This result is in agreement with the work of Wan *et al.*,[24] concerning the assembly mechanisms in relation to the organic chain length of the capping agent. Moreover, an inter-particle spacing (edge-to-edge) of approximately 3 nm was derived as $\Delta = a - D_{Au}$.

In situ GISAXS investigation of PbS QD superlattices

Two sets of PbS QD samples, dispersed in toluene, with average size of 2.7 nm and 3.3 nm, at three different QD concentration values, namely 3×10^{-7} M, 5×10^{-7} M and 7×10^{-7} M, were drop-cast onto Si substrate and the solvent was left to evaporate at room temperature. Similarly, small volumes of the same QD dispersions were drop-cast on copper TEM grids.

The investigated concentration range was selected on the basis of previous findings, to be above the critical concentration corresponding to the minimum value of entropic gain associated to the release of free volume in the QD solution during the evaporation process and necessary to overcompensate the entropic loss due to the ordering in the lattice structure.[18] The TEM micrographs of the different samples (ESI,† Fig. S1), show the tendency of the QDs to self-organize according to a hexagonal arrangement, for both QD sizes, at any investigated concentration.

In situ GISAXS experiments were performed on the two sets of size-monodispersed PbS QDs, to investigate the structural evolution of the assemblies during solvent evaporation, and thus obtain insight on the early stages of the superstructure formation process. The whole evaporation process was monitored, up to 30 min. Fig. 4 shows the *in situ* GISAXS patterns collected for $PbS_{2.7}$ (a–c panels) and $PbS_{3.3}$ (d–f panels) QDs, at increasing concentration of the drop cast QD solution, during solvent evaporation. For each sample the earliest frame featuring any scattering signal from the samples is reported, being *ca.* 10 s for $PbS_{2.7}$ and about 15 min for $PbS_{3.3}$.

Fig. 5 shows the last GISAXS frame, collected about 30 min after the QD solution deposition (ESI,† Movies 4–9). Differently from the case of Au NP assemblies, diffraction rings and spots appear in the GISAXS patterns from PbS assemblies, clearly indicating the formation of 3D assemblies. The patterns (Fig. 5) have been indexed by using the software NANOCELL.[25] The fcc symmetry was recognized as the only superlattice symmetry present in both $PbS_{2.7}$ and $PbS_{3.3}$ series, with (111) preferential orientation, but with different degrees of order. In Fig. 5, circles and relevant index mark the positions of the intensity maxima calculated by NANOCELL, and were kept in all of the panels as a reference. The distribution of the scattering intensity does never deviate from what expected for an fcc structure, although the diffraction features appear less pronounced at increasing QD concentration. It is worth to note that, differently from what observed for Au NP assemblies, the increase in QD concentration results in a lower degree of assembly order, for both PbS QD size samples. Such a trend is more evident for the $PbS_{3.3}$ series, where the superlattice signals are almost lost in the intermediate concentration sample (Fig. 5e), and a broad isotropic correlation ring appears instead; whereas in the highest concentration sample (Fig. 5f) a powder-like fcc superlattice structure, with no clear preferential orientation, is observed.

Interestingly, for $PbS_{2.7}$ the real time GISAXS data show that partial diffraction rings in the direction perpendicular to sample surface emerge already in the early frames (Fig. 4a–c), at *q*-values corresponding to the (111) and (002) planes of the fcc superlattice (clearly visible in the Fig. 5). These evidences suggest that the 2.7 nm QDs start assembling earlier, with respect to $PbS_{3.3}$, in oriented layered structures with the characteristic repeat distances of the (111) and (002) fcc

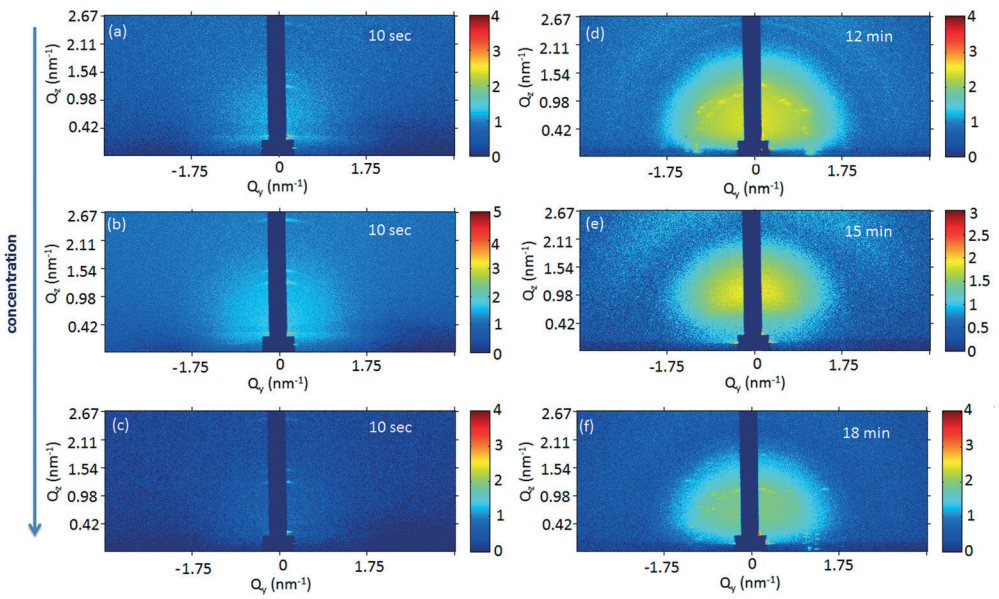

Fig. 4 GISAXS patterns collected during solvent evaporation for $PbS_{2.7}$ (a–c panels) and $PbS_{3.3}$ (d–f panels) for increasing QD solution concentration, as indicated by the arrow on the left. For each sample the earliest frame featuring any scattering signal is reported.

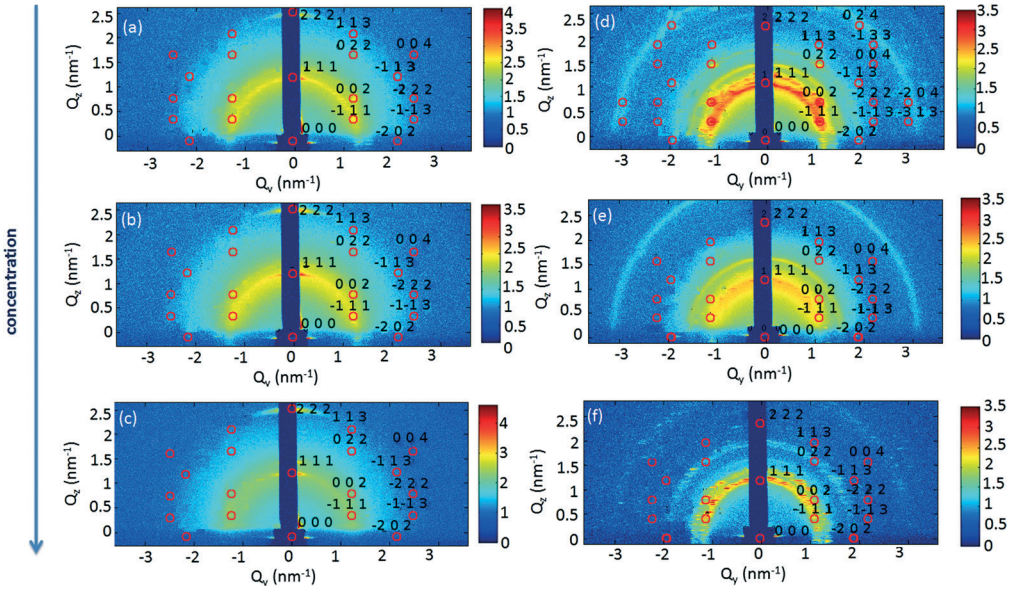

Fig. 5 GISAXS patterns collected from $PbS_{2.7}$ (a–c panels) and $PbS_{3.3}$ (d–f panels) assemblies obtained by evaporation at increasing concentration. For each sample the last frame (30 min) is reported and indexed as (111)-oriented fcc superlattice.

superlattice planes. The particular orientation of such layers (preferentially parallel to the substrate) indicates that the superlattice starts forming along a flat surface, at the solution substrate interface; only afterwards, in the late stage of the solvent evaporation (Fig. 5a–c), the *translational* order of the stacked QDs also extends in the direction parallel to the substrate, leading to the 3D superlattice formation. On the contrary, in the case of $PbS_{3.3}$ samples, no layered structures were detected in any of the early stage frames (Fig. 4d–f): the superlattice formation proceeds with in plane and out of plane correlation features appearing concomitantly (Fig. 5d–f), eventually leading to 3D superlattices with different degrees of order, as shown in the last collected frames (Fig. 5d–f).

For both QD sizes, and for all the initial drop cast solution concentration values, the unit cell parameters were calculated from the (111) *d*-spacing: $a(PbS_{2.7})$ = 8.6 nm and $a(PbS_{3.3})$ = 9.5 nm. Accordingly, nearest-neighbour distance of 6.1 and 6.7 nm were found for $PbS_{2.7}$ and $PbS_{3.3}$, respectively, hence scaling with the QD diameter. The same 3.4 nm inter-particle (edge-to-edge) separation was derived for both $PbS_{2.7}$ and $PbS_{3.3}$ samples.

In addition, in the case of the $PbS_{3.3}$ samples, besides the main fcc superlattice structure, two continuous rings, not crossing any of the fcc diffraction spots, appear in the GISAXS maps, corresponding to a repeat distance of 4.0 nm, whose attribution needs further measurements. Such additional lamellar phases cannot be excluded for the $PbS_{2.7}$ series, in case of high preferential orientation in the direction perpendicular to the sample plane, as they would probably be hidden behind the beam stopper.

GISAXS *ex situ* studies on aged PbS QD superlattices

GISAXS measurements were carried out *ex situ* on the aged *assemblies* and the obtained results were compared with those achieved from assemblies prepared by drop casting the aged *solutions*. GISAXS 2D maps, collected at a 180 mm distance on the aged *assemblies* are reported in Fig. 6a–b (and full range in ESI,† Fig. S2a–b) for $PbS_{2.7}$ and $PbS_{3.3}$, respectively. The superimposed indexing shows that the fcc symmetry

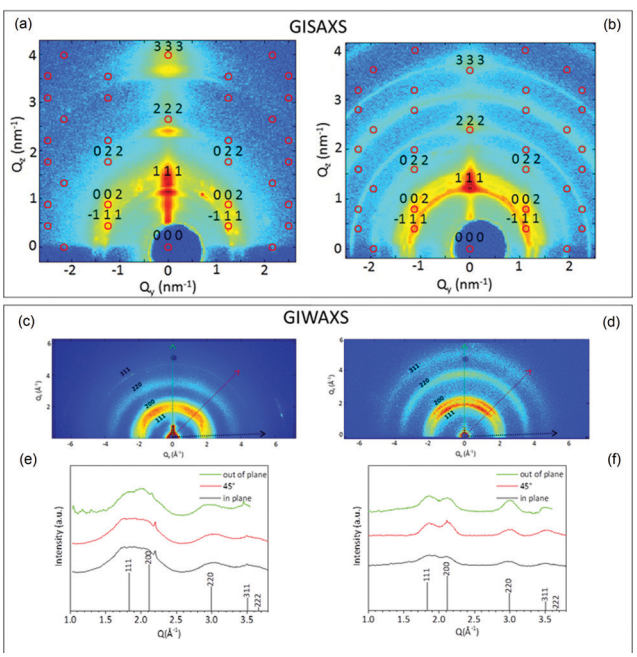

Fig. 6 2D experimental maps from *ex situ* GISAXS measurements on $PbS_{2.7}$ (a) and $PbS_{3.3}$ (b) assemblies after aging in air (aged *assemblies*), indexed as fcc superlattices; 2D (c, d) and 1D (e, f) experimental data from *ex situ* GIWAXS measurements on the $PbS_{2.7}$ and $PbS_{3.3}$ samples, respectively. The 1D profiles are taken along the arrows marked on the 2D maps with relevant colours. The reference pattern of the rock-salt PbS structure is also reported below the 1D profiles.

is retained in both QD size assemblies, even after aging in air. On the other hand, a unit cell contraction of approximately 10% for $PbS_{2.7}$ and 7% for $PbS_{3.3}$, with corresponding cell parameters of 7.7 and 8.8 nm, respectively, was found in the aged samples. The different results obtained for the interparticle distances in superlattices, prepared by fresh and aged solution, can be attributed to oxidation phenomena on QDs. Indeed, QD cores are supposed to reduce their size, *e.g.* for oxidation phenomena, while exposed to air, like in the investigated case.[26]

A comparison between vis-NIR absorption spectra recorded on the original solution used for the earlier *in situ* samples and on the same sample after 7 months, revealed only a slight difference in wavelength of the first 1S excitonic transition, as the exciton feature of $PbS_{2.7}$ and $PbS_{3.3}$ moves toward blue of 12 nm and 26 nm, respectively (data not reported). Such blue-shift is in agreement with a possible surface oxidation of the QDs. Indeed, the formation of a very thin layer of oxide on PbS QD surface determines a reduction of the actual size of the crystalline core. However, for the aged samples, the calculated size values obtained from the absorption measurements[20] indicate only a negligible reduction of the crystalline core size. On the other hand, edge-to-edge interparticle spacing of 2.9 and 3.0 nm for $PbS_{2.7}$ and $PbS_{3.3}$ aged superlattices, respectively, obtained by GISAXS, correspond to a reduction of about 0.4 nm with respect to the spacing in the fresh assemblies. Such a reduction can be eventually ascribed to a cell contraction due to the aging of both assemblies and solutions, which can be responsible for the lower interparticle distance.[27]

GIWAXS measurements were also performed, to account for a possible QD *orientational* order. GIWAXS 2D frames (Fig. 6c–d) and the cuts taken along the arrows marked in the 2D maps with relevant colours (Fig. 6e–f) are displayed: in plane (black curve), out of plane (green curve) and at 45° (red curve). This comparison does not show relevant differences for $PbS_{2.7}$ sample, either in terms of peak intensity and FWHM and evidences an isotropic almost spherical shape and no preferential orientation of the QDs. Conversely, comparing the FWHM of the (111) and (220) peaks for the $PbS_{3.3}$ sample, in Fig. 6f, they are slightly different as in the case of not fully isotropic QD shape. Furthermore, QDs hold a slight *orientational* order in this sample, with the (220) planes preferentially oriented parallel to the substrate: *i.e.* the QD superlattice is 111-oriented and its QD building blocks are 110-preferentially oriented.

To better investigate the influence of QD concentration on superlattice formation, assemblies of PbS QD aged *solutions* with further diluted concentrations were prepared. GISAXS measurements were performed for sample $PbS_{2.7}$, by drop-casting on a substrate QS solutions with concentrations equal to 3×10^{-8} M, 3×10^{-9} M, 3×10^{-10} M, respectively. The measurements indicate that, even in case of so reduced QD concentrations, the formation of 3D fcc domains is always observed, although with much lower scattering signal, thus demonstrating the high tendency of PbS QDs to form 3D superstructures, differently from what observed in the case of Au NPs. The GISAXS experimental pattern of a 3×10^{-9} M PbS QD sample is reported in ESI,† Fig. S3. Indexing of GISAXS patterns, collected at 2 m distance from the sample, was then also performed on the same aged *assemblies* in order to enhance resolution and thus allow a more precise evaluation of the cell parameter values (data not shown). This set of measurements resulted in calculated nearest-neighbour distances of 5.4 and 6.2 nm, slightly different from those found on the original fresh assemblies.

The GISAXS pattern (collected at ~2 m sample-to-detector distance) obtained from the low concentration $PbS_{2.7}$ aged *solution* is reported in ESI,† Fig. S4, where simulations of the fcc diffraction pattern for different orientations of the superlattice have been superimposed, ascribing the intensity variation mainly to a mosaic of (111) preferentially oriented fcc superlattices, rather than different superlattice symmetries. GISAXS patterns from the aged *assemblies* (Fig. 6a–b, as well as Fig. S2a–b†) show an additional scattering from lamellar phases, for both samples. These lamellae result randomly oriented in the $PbS_{3.3}$ aged sample, and highly oriented in the $PbS_{2.7}$ aged sample, which mainly give scattering perpendicular to sample surface ($Q_y = 0$). While the 4.0 nm lamellar phases were formed along with the QD superlattices at the early stages of the evaporation process and are still present in the aged *samples*, newly detected lamellar structures, characterized by a 5.0 nm periodicity, were clearly formed at a much later stage, and probably ascribable to an aging effect, whose nature needs to be further clarified.

Discussion

In the first stage of the superlattice formation, NPs can be considered as uniformly suspended within the solution droplet. When the solvent starts to evaporate, a local increase of particle concentration occurs immediately beneath the liquid surface, due to the faster evaporation of solvent at the surface, with respect to the nano-object diffusion speed in the solution. This can produce the formation of a NP monolayer at the liquid surface, which is stabilized by surface tension. If this condition of supersaturation persists, with the progressive solvent evaporation, a second NP layer can form, above the first layer, and so on until the drop liquid surface reaches the substrate.[28] Interestingly, these stacked layers (*lamellae*) can eventually merge, to form large area superstructures, on the air–liquid interface. After the solvent evaporation, this NP layer(s) will deposit on the substrate.[29]

During the solvent evaporation, the progressive NP organization is driven by a delicate balance among many contributions, such as Coulomb interaction, dispersive van der Waals forces, or charge-dipole, dipole–dipole and charge-induced dipole interactions. These contributions depend on many factors, as NP chemical composition, type and length of capping molecule and so on. A narrow size distribution is fundamental to obtain highly regular and surface extended NP superlattice with an ordered geometry, hence a high translational order, although even in a narrow size distribution the QD

size can still slightly vary. The interaction between NPs is mediated by the organic coordinating molecules, whose composition and length can control NP interparticle distance, resulting not only in *translational*, but also *orientational* order, which is possible when faceted NPs arrange following a specific mutual orientation.

Summarizing the major results of the GISAXS and GIWAXS analysis on Au NPs and PbS QDs we found that: i) the Au NP assembly produces a superlattice symmetry approximately hexagonal, that does not change as a function of concentration, in the investigated range. The assembly proceeds forming 2D islands parallel to the substrate plane, without the formation of layered 3D nanostructures. ii) For PbS QD superlattice formation, both sizes of QDs organize themselves in oriented layered structures with the characteristic repeat distances of the (111) and (002) fcc superlattice planes. It is worth to note that $PbS_{2.7}$ starts assembling earlier with respect to $PbS_{3.3}$. In the case of $PbS_{3.3}$ sample, no single layered structures can be detected in any of the early stage frames but in-plane and out-of-plane superlattice 3D correlation features appears concomitantly (*translational* order). iii) The $PbS_{2.7}$ are more spherical in shape and do not show any preferential orientation; whereas $PbS_{3.3}$ are with slightly anisotropic shape and 110-preferentially oriented (*orientational* order). iv) GISAXS measurements on both aged *assemblies* and aged *solutions* demonstrated that the fcc symmetry is retained for both QD size assemblies with unit cell contraction with respect to the fresh prepared superlattices. v) Lamellar phases are also formed and randomly oriented in the $PbS_{3.3}$ QD aged sample, by highly oriented in the $PbS_{2.7}$ sample.

In the case of the spherical Au NPs, during the solvent evaporation, two contributions have to be mainly considered: the Coulomb interparticle interaction and the low chemical affinity between the long alkyl chain of OAm molecules capping the NPs and the thin layer of SiO_2 naturally occurring on Si substrates, when handled in normal conditions. For what concerns the first contribution, Au NPs undergo reciprocal repulsive Coulomb interaction, as it is well known that, in presence of OAm, a weak electrical charge is present on the sterically stabilized nanoparticles, even in non-polar solvents.[30] In this condition, during the NP assembly, an accumulation of non-compensated charges will be experienced, that induce the formation of many small domains that simultaneously nucleate on the silicon substrate, thus inhibiting the NP 3D superstructure growth. In addition, Au NPs tend to minimize the contact area with the SiO_2/Si substrate, due to the low chemical affinity between the polar SiO_2 surface and the hydrophobic alkyl chain of OAm molecules coordinating NP surface, as recently demonstrated,[10] thus reducing the probability to uniformly distribute onto the SiO_2 film coating the substrate.

In the case of PbS QDs, the chemical composition of the capping molecules can be considered similar to that of Au NPs, being OAm and OAc characterized by the same long alkyl chain. Thus, the different behaviour between the two assembled systems can be ascribed to the different chemical composition, and specifically to the different energetic interaction between the NPs, as well as to the diverse NP size and shape. Differently from metal NPs, semiconductor QDs exhibit large dipole moment and polarizability which also influence their interparticle interaction during the superlattice formation. These contributions become very important for PbS QDs, which are characterized by a very large dipole moment.[31] The strong dipoles is believed to arise from an uneven distribution of Pb and Se terminated {111} facets of individual QDs or charged surface states. The distribution of dipolar moments are also related to the QD shapes. With increasing the size of the growing superstructure, the further orientation of dipoles becomes energetically favoured, because of a larger mutual connectivity of dipole moments. Indeed, every new QD joining the existing arrangement of the dipoles will follow the geometrical pattern dictated by the underlying lattice, even though less energetically favourable.[32] Instead, for what concerns the Coulomb contribution, the presence of both OAc and TOP molecule on PbS QD surface allows to reasonably think that QD surface charge is almost neutral. Indeed, the literature reports that PbS QD surface charge can be modified by adding surfactant molecules like carboxylic acids (which increases the population of negatively charged QDs) and tri-nalkylphosphine oxides/tri-nalkylphosphines (which, conversely, increases the population of positively charged QDs).[33] Thus the repulsive Coulomb potential between adjacent QDs in the growing superlattice can be considered negligible. This is a further factor which contributes to stabilize QD superstructures with high extension and long-range order.

Also the QD assembling in a periodic packing is unavoidably affected by particle size and shape. From our findings, two competitive forces leave a direct fingerprint in the assembly of PbS QDs: the QD shape and the distribution of the capping molecules. The assembly of $PbS_{2.7}$ (as reported in Fig. 6e) is not driven by the particle shape. Oriented layered structures form directly at the early stages of the solvent evaporation, with the characteristic repeat distances of the (111) and (002) fcc superlattice planes, and also lamellar phases are measured with a strong preferred orientation. Indeed, for smaller QDs whose shape can be approximated as spherical, the distribution of the alkyl chains on the surface is likely to be uniform without bundle formation. However, for larger and faceted particles the uniform passivation model may not works properly, as the capping molecules may be not uniformly distributed on QD surface. In the case of $PbS_{3.3}$ sample, where GIWAXS data indicate QDs with anisotropic shape and preferred orientation (as reported in Fig. 6f), their faceted surfaces can direct the coordination of OAc and TOP molecules not uniformly, and drive them to concentrate at the QD surfaces, edges or corners.[28] In this situation, the capping molecules are bundled on QD facets, and can geometrically direct the QD aligning by mutually exposing specific faces. The capping molecules interconnect the facets of QDs, serving as the binding force that holds the

particles together to form a 3D lattice. From the structural point of view, these molecular bonds tend to align the facets on which they are connected in a parallel (face-to-face) fashion. Then the different time measured to obtain the first evidence of superlattice formation between $PbS_{2.7}$ and $PbS_{3.3}$ could be correlated to the longer time necessary to $PbS_{3.3}$ to orient the QD faces. From a geometrical point of view, in case of faceted QDs, the matching between neighbouring QDs could be explained by a gear model, in agreement with preferred orientation and anisotropic shape of the QDs, in which the bundled capping molecules behave as teeth in a gear in driving the QD assembly.[34]

Conclusions

In this work the combined structural approach of *ex situ* electron microscopy with *in situ* GISAXS investigation and *ex situ* GISAXS/GIWAXS has provided a fundamental contribution for understanding the process underlying the formation of NP assembly, upon solvent evaporation. Particularly, this study focused on the role played by NP concentration and chemical composition on the overall assembly formation.

Two different systems, based on OAm capped Au NPs and OAc-capped PbS QDs have been investigated, demonstrating how the signatures of the superlattices at various stages of the self-assembly process, since their early stage of formation, are different for the two types of samples. The two systems show a significantly different behaviour, as in the case of Au NPs in the investigated range of concentration the assembly proceeds in 2D layer, due to the contribution of both Coulomb repulsion and interaction with the substrate. Conversely, the results obtained investigating the formation of assemblies of OAc-capped PbS QDs indicate that the formation of 3D fcc superlattices is driven by the different chemical composition, and specifically to the different energetic interaction between the QDs, which can be mainly ascribed to their large dipole moment and polarizability (*translational order*). In addition, the shape of QDs and to the possible not isotropic distribution of the molecular ligand on QD surface for the larger and faceted NCs, has been found to play a decisive role on the final superlattice *orientational* order.

In conclusion, the role of NP capping molecules can be described not just in a mere control of interparticle distance, but, remarkably also in the careful definition of their *orientational* order, and in a significant energetic contribution to the nucleation and growth process of NP supercrystals. Air-aging effects were also investigated, and a unit cell contraction was found relative to the fresh assembled structures, whereas no symmetry changes were observed.

Acknowledgements

This work was partially supported by Italian National Consortium for Material Science and Technology (INSTM), by MAAT PON project (CUPB31C12001230005, "Molecular Nano-technology for Health and Environment"), by the FIRB 2009/2010 project "Rete integrata per la Nano Medicina (RINAME)" – RBAP114AMK_006, by the project Nanomax-integrable sensors for pathological biomarkers diagnosis (N-CHEM), by PRIN 2012 Italian National Project (Prot. 2012T9XHH7) and CNPq (490517/2011-0). LNLS is acknowledge for the access to the XRD2 beamline. Rocco Lassandro and Caterina Chiarella are acknowledged for their support to the XMI-LAB, Douglas Henrique Caetano de Araujo and Henrique Ferreira Canova for their technical support at the XRD2 beamline at LNLS.

Notes and references

1 T. Hanrath, J. J. Choi and D.-M. Smilgies, *ACS Nano*, 2009, **3**, 2975.
2 S. Jayaraman, L. T. Yua and M. P. Srinivasan, *Nanoscale*, 2013, **5**, 2974.
3 M. I. Bodnarchuk, M. V. Kovalenko, S. Pichler, G. Fritz-Popovski, G. Hesser and W. Heiss, *ACS Nano*, 2010, **4**, 423.
4 K. J. M. Bishop, C. E. Wilmer, S. Soh and B. A. Grzybowski, *Small*, 2009, **5**, 1600.
5 N. A. Kotov, *J. Mater. Chem.*, 2011, **21**, 16673.
6 H. Tong, N. Umezawa, J. Ye and T. Ohnoc, *Energy Environ. Sci.*, 2011, **4**, 1684.
7 Y. Caia and H. Fan, *CrystEngComm*, 2013, **15**, 9148.
8 D. A. Kalashnikov, Z. Pan, A. I. Kuznetsov and L. A. Krivitsky, *Phys. Rev. X*, 2014, **4**, 011049.
9 M.-H. Lin, H.-Y. Chen and S. Gwo, *J. Am. Chem. Soc.*, 2010, **132**, 11259.
10 M. Corricelli, N. Depalo, E. Fanizza, D. Altamura, C. Giannini, D. Siliqi, R. Di Mundo, F. Palumbo, V. G. Kravets, A. N. Grigorenko, A. Agostiano, M. Striccoli and M. L. Curri, *J. Phys. Chem. C*, 2014, **118**, 7579.
11 M. Corricelli, F. Enrichi, D. Altamura, L. De Caro, C. Giannini, A. Falqui, A. Agostiano, M. L. Curri and M. Striccoli, *J. Phys. Chem. C*, 2012, **116**, 6143.
12 T. Franzl, T. A. Klar, S. Schietinger, A. L. Rogach and J. Feldmann, *Nano Lett.*, 2004, **4**, 1599.
13 P. Siffalovic, E. Majkova, L. Chitu, M. Jergel, S. Luby, A. Satka and S. V. Roth, *Phys. Rev. B: Condens. Matter Mater. Phys.*, 2007, **76**, 195432.
14 F. Pietra, F. T. Rabouw, W. H. Evers, D. V. Byelov, A. V. Petukhov, C. de Mello Donegá and D. Vanmaekelbergh, *Nano Lett.*, 2012, **12**, 5515.
15 H. Hiramatsu and F. E. Osterloh, *Chem. Mater.*, 2004, **16**, 2509.
16 E. Fanizza, N. Depalo, L. Clary, A. Agostiano, M. Striccoli and M. L. Curri, *Nanoscale*, 2013, **5**, 3272.
17 X. Liu, M. Atwater, J. Wang and Q. Huo, *Colloids Surf., B*, 2007, **58**, 3.
18 M. Corricelli, D. Altamura, L. De Caro, A. Guagliardi, A. Falqui, A. Genovese, A. Agostiano, C. Giannini, M. Striccoli and M. L. Curri, *CrystEngComm*, 2011, **13**, 3988.
19 D. Altamura, R. Lassandro, F. A. Vittoria, L. De Caro, D. Siliqi, M. Ladisa and C. Giannini, *J. Appl. Crystallogr.*, 2012, **45**, 869.

20 I. Moreels, K. Lambert, D. Smeets, D. De Muynck, T. Nollet, J. C. Martins, F. Vanhaecke, A. Vantomme, C. Delerue, G. Allan and Z. Hens, *ACS Nano*, 2009, **3**, 3023.
21 P. J. Thistlethwaite and M. S. Hook, *Langmuir*, 2000, **16**, 4993.
22 K. A. Abel, J. Shan, J.-C. Boyer, F. Harris and F. C. J. M. van Veggel, *Chem. Mater.*, 2008, **20**, 3794.
23 A. Lobo, T. Moller, M. Nagel, H. Borchert, S. G. Hickey and H. Weller, *J. Phys. Chem. C*, 2005, **109**, 17422.
24 Y. F. Wan, N. Goubet, P. A. Albouy and M. P. Pileni, *Langmuir*, 2013, **29**, 7456.
25 M. P. Tate, V. N. Urade, J. D. Kowalski, T. C. Wei, B. D. Hamilton, B. W. Eggiman and H. W. Hillhouse, *J. Phys. Chem. B*, 2006, **110**, 9882.
26 I. Moreels, Y. Justo, B. De Geyter, K. Haustraete, J. C. Martins and Z. Hens, *ACS Nano*, 2011, **5**, 2004.
27 S. Xiong, D. R. Dunphy, D. C. Wilkinson, Z. Jiang, J. Strzalka, J. Wang, Y. Su, J. J. de Pablo and C. J. Brinker, *Nano Lett.*, 2013, **13**, 1041.
28 Z. L. Whang, *Adv. Mater.*, 1998, **10**, 13.
29 T. P. Bigioni, X.-M. Lin, T. T. Nguyen, E. I. Corwin, T. A. Witten and H. M. Jaeger, *Nat. Mater.*, 2006, **5**, 265.
30 P. de la Presa, M. Multigner, J. de la Venta, M. A. García and M. L. Ruiz-González, *J. Appl. Phys.*, 2006, **100**, 123915.
31 Z. Tang, N. A. Kotov and M. Giersig, *Science*, 2002, **297**, 237.
32 D. V. Talapin, E. V. Shevchenko, C. B. Murray, A. V. Titov and P. Král, *Nano Lett.*, 2007, **7**, 1213.
33 E. V. Shevchenko, D. V. Talapin, N. A. Kotov, S. O'Brien and C. B. Murray, *Nature*, 2006, **439**, 55.
34 Z. L. Whang, *Mater. Charact.*, 1999, **42**, 101.

